Evaluation of hours-ahead solar forecasting using satellite imagery and Numerical Weather Prediction

Chi Wai Chow[1], Juan Luis Bosch[1], Jan Kleissl[1]
[1]Department of Mechanical and Aerospace Engineering, University of California, San Diego

Executive Summary

A method for solar forecasting using cloud motion vectors (CMV) from satellite imagery with the ability to characterize forecast uncertainty has been developed. On average, the root mean square error (RMSE) for CMV forecast increases with increasing forecast horizon and becomes larger than the North American Model (NAM, a numerical weather prediction model) forecast error at between 6 hours and 1 day. Consequently, satellite CMV forecasts are superior for short time horizons and they are currently used as the model of choice in SolarAnywhere forecasts up to a 6 hour horizon. However, the forecast horizon at which the 'crossover' between CMV and NAM occurs is dynamic (as short as 2 hours) and could be adjusted if the CMV forecast certainty was known at forecast issue time. The RMSE of CMV forecasts was most related to satellite image entropy and uniformity. The relative performance (RP), i.e. the ratio of the errors of NAM and satellite CMV forecast is also analyzed. The average rRMSE of predicting RP is shown to be about 30% for two different modeling techniques. The models and metrics developed in this project can be applied to choose the optimal forecast model and reduce solar forecast errors especially for hour-ahead forecasts. An operational CMV forecast can be produced with a 25 minute latency.

1. Introduction

Hours-ahead solar forecasting is important for grid operators to manage intra-day solar variability through procurement of reserves and operation of energy markets. As Geostationary Operational Environmental Satellite (GOES-15) was deployed last year and the more advanced GOES-R will be launched in 2017, the ability of solar forecasting using satellite imagery is expected to improve and to be widely used by forecast providers.

In this study, a technique for solar forecasting using satellite imagery with the ability to characterize and predict forecast error is presented. Many forecast techniques have been developed for solar irradiance using satellite imagery and Numerical Weather Prediction (NWP) (e.g. Hammer et al, 2000, Perez et al., 2010, 2011, Marquez et al., 2012). Perez et al (2010) showed that the satellite cloud motion-based forecasts improve upon NWP forecasts up to forecast horizons of 4-5 hours on average over the United States. For operational forecasting, however, the relative skill of different forecasts depends on meteorological conditions. The motivation of this study is to determine this "cross-over time" under different conditions and determine parameters (cloud cover fraction, cloud speed, etc.) that are good predictors for this cross-over time.

For NWP, good predictors of solar irradiance forecast error are clear sky index and solar zenith angle (Lorenz et al., 2009, Mathiesen and Kleissl, 2011). For satellite forecasts no published results on predictors of error exist. Knowledge of the cross-over time and determining parameters will allow the composition of a forecast across all time horizons, which is based on optimal combinations of inputs from different models. For example, a satellite model would be chosen as the forecast if it had been determined to be most accurate for frontal passages with homogeneous cloud cover and persistent cloud motion. More accurate and certain solar forecasts would facilitate more economical high solar penetration on the electric grid. In section 2, we describe the data set in this study. In section 3, the cloud motion vector method is introduced (3.1) and characteristic image features are defined (3.2). Also, multivariate linear regression and analog models are described. In section 4, overall NWP and CMV model performance is quantified (4.1) and then CMV errors are related to satellite image features qualitatively (4.2) and through linear regression models (4.3). Finally, section 4.4 analyzes the predictability of the relative performance of NWP and CMV forecasts using linear regression and analog methods. Conclusion are presented in section 5.

2. Data

2.1 Goes-15 Imager data

The Geostationary Operational Environmental Satellite-15 (GOES-15) Multispectral Imager satellite dataset from April 24th to May24th is used. GOES-15 generates a full disk image every 15 minutes with a spatial resolution of 1km and 4km for the visible and infrared bands, respectively. All of our results are presented at 4 km resolution. The domain of interest covers an open ocean region with an approximate size of 2000 km x 2000 km from $32°22'$ to $34°31'$ N and from $122°62'$ to $127°62'$ W (Fig 1). Open ocean area is selected to avoid complex terrain effects that introduce stationary (mountain) clouds and high spatial variability in satellite measured reflectivity. GOES-15 images starting at 1645 and 1700 UTC (09 PST) are used to determine cloud speed and the 1700 UTC cloud transmission image is advected with hourly time steps out to a forecast horizon of 6 hours.

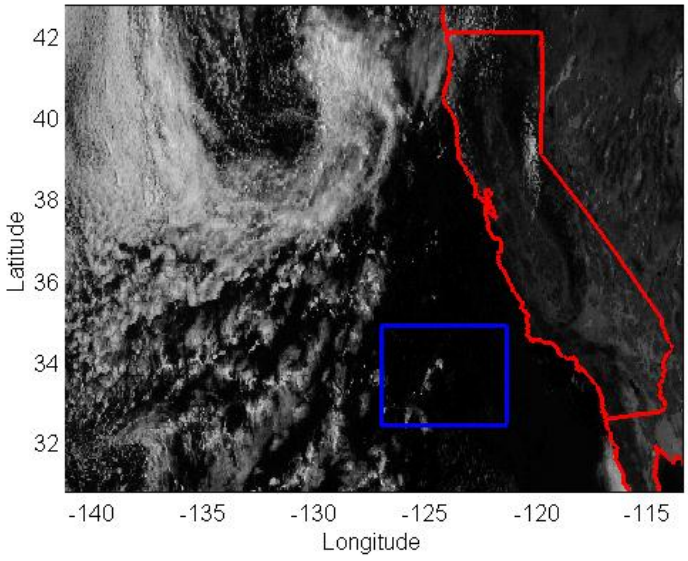

Figure 1. GOES-15 visible channel image that shows the region of interest (blue) with the coast and California state lines (red).

2.2 CLAVR-x

The GOES-15 data is processed with the CLAVR-x algorithm developed by the GOES-R Advanced Baseline Imager (ABI) Cloud Algorithm Working Group (AWG) to provide cloud-related information. CLAVR-x generates cloud masks and classifies clouds into different types such as water, supercooled water, mixed phase, cirrus, opaque ice, etc (Pavolonis et al 2004, 2005). Among over thirty variables, cloud transmission and cloud mask with 4 km spatial resolution from the CLAVR-x are used. Assuming the atmosphere without clouds is transparent to the global horizontal irradiance (GHI), cloud transmission can be approximated as the clear sky index defined as

$$kt = \frac{GHI_{measured}}{GHI_{clear\ sky}}, \quad (1)$$

where $GHI_{clear\ sky}$ is computed using a clear sky model that depends on location, time, elevation, and Linke turbidity (Ineichen and Perez, 2002). Since the spatial resolution and coordinate system is different between GOES-15 and NAM data. GOES-15 data is up-scaled and collocated with the NAM by simple averaging and linear interpolation.

2.3 North American Mesoscale Model (NAM)

The total downward short wave radiation (GHI) from the NAM forecast is published by the National Oceanic and Atmospheric Administration's (NOAA) NCEP with a 12 km x 12 km grid spanning the continental United States (CONUS). Forecasts published at 12 UTC (shortly before sunrise at the region of interest) with hourly time steps out to 36 hours are used. Forecast kt is computed as in Eq. (1). Since satellite forecast issue time is 1700 UTC (Section 2.1), the sixth hour of the NAM forecast is compared to the first hour of satellite forecast and so on. Since the NAM forecast error varies only weakly in time for the first 24 hours (Perez et al., 2009), the difference in forecast horizon is not expected to impact the results.

3. Methods

3.1 Cloud Motion Vectors Forecast

Atmospheric motion vectors (AMV) have been derived from geostationary satellites since the 1960s (Fujita 1968) and different tracers and meteorological scales have been selected to derive AMV. In this paper, the cloud transmission or kt is used as a tracer. The cross-correlation method (CCM) and two consecutive (15 min apart) kt images are utilized to derive cloud motion vectors (CMVs). A 15 x 15 pixels (60 x 60 km) target box is used to cross-correlate within a 100 x 100 km search box (Fig. 2). This limits the maximum detectable velocity to 200 km h^{-1}. To increase the computational efficiency, CCM only computed at 12 km resolution (every 3 pixels).

Assuming kt and CMVs remain constant over the forecast horizon, computed pixel-by-pixel CMVs are used to advect the kt pixels to each forecast horizon (Fig. 2). Nearest neighborhood interpolation is applied on sections of the forecast kt image where gaps and overlapping pixels are introduced by converging and diverging flow.

Two quality control procedures are applied. First, CMVs in cloud-free regions (as per the CLAVR-x cloud mask) are removed. Second, AMVs that significantly differ from the neighboring vectors are replaced using a median filter technique. These vectors might represent errors in the cross-correlation algorithm or (less likely) depict actual local (microscale) motion associated with convective clouds (Mecikalski 2002; Rabin et al. 2004). The objective is to estimate hours-ahead cloud motion, therefore, small scale convective (and short-lived) cloud motion (as considered for example in Nieman et al. (1997), Velden et al. (1997, 1998)) is neglected here.

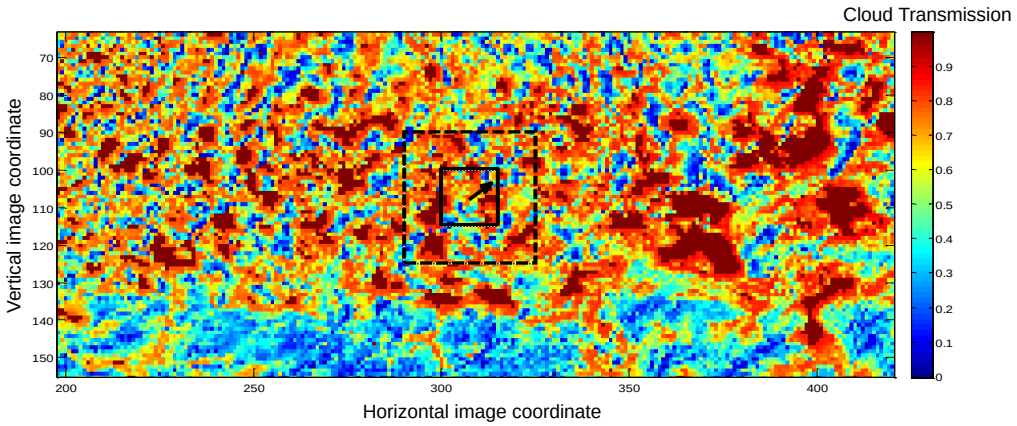

Figure 2. Illustration of CCM on an image of cloud transmission (4 km resolution) at 10 PST on 7th June, 2012. A 60 x 60 km pixels target box (solid black line) is cross-correlated within a 100 x 100 km pixels search box (dash black line) from a cloud transmission image 15 minutes later (not shown here). A cloud motion vector is obtained for the center pixel of the target box.

3.2 Features

Seven different regional features (Table 1) extracted from the forecast kt maps are used to characterize the CMV and NAM forecast error. For CMV forecast, spatially averaged cloud speed, kt (AVGKT), correlation coefficient (CC) obtained as described in section 3.1, standard deviation of kt (std), cloud fraction (Cf from CLAVR-x), entropy, and uniformity are computed over the domain (Fig. 1) to represent the state of atmosphere (Fig. 3). All features are computed on the forecast kt image to account for likely local conditions at the forecast valid time. For NAM, the same forecast features are computed except cloud speed, std, and CC.

Table 1. Regional features that are extracted from the forecasted kt image and used as the predictors of CMV and NAM forecast error.

Regional Features	Formula	Description and Relevance
Cloud fraction (Cf)	$\frac{\#\ of\ cloudy\ pixels}{\#\ of\ pixels}$	An image with a very small or very large cloud fraction (clear or overcast) is easier to forecast
Cloud Speed	$\sum_{i=1}^{n} p(cs_i)cs_i$	cs_i is the cloud speed of each pixel, p is the probability of cs_i, and n is the number of pixels in an image. An image with higher cloud speed would be more difficult to forecast since error in cloud direction will cause clouds to diverge faster from

Table 1. Regional features that are extracted from the forecasted kt image and used as the predictors of CMV and NAM forecast error.

Regional Features	Formula	Description and Relevance
		their actual position.
Correlation Coefficient (CC)	$\sum_{i=1}^{n} p(cc_i)cc_i$	Spatially averaged cross-correlation coefficient measuring the degree of correspondence between the 1645 and 1700 images that are used to determine CMVs (Haralick et al, 1992). An image with smaller CC indicates larger shape or cover changes in the cloud field making CMVs less accurate and violating the assumption of a 'frozen' cloud field. Reduced forecast accuracy would result.
AVGKT	$\sum_{i=1}^{n} p(kt_i)kt_i$	Spatially averaged cloud transmission.
Std	$\sqrt{\sum_{i=1}^{n} p(kt_i)(kt_i - \langle kt_i \rangle)^2}$	Average contrast of an image (see Fig. 3). For the same Cf an image with larger std would be more difficult to forecast.
Entropy	$\sum_{i=1}^{n} p(kt_i)log_2 p(kt_i)$	Randomness of an image (see Fig. 3). For the same std an image with larger Entropy would be more difficult to forecast.
Uniformity	$\sum_{i=1}^{n} p(kt_i)$	Uniformity in image pattern (see Fig. 3). For the same Cf an image with smaller Uniformity would be more difficult to forecast.

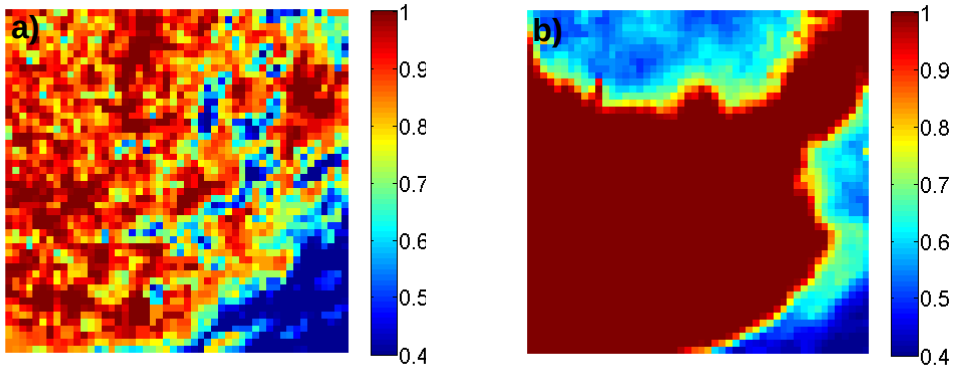

Std:	0.19	0.19
Entropy:	0.134	0.07
Uniformity:	0.0122	0.069

Figure 3. Illustration of two different kt (colorbar; blue: thick clouds, red: clear) patterns. Both (2000 x 2000 km) images have the same average contrast (std) but different entropy and uniformity. The high entropy kt image (a) shows a random cloud field, while the low entropy kt image (b) shows a clear sky with a two well defined clouds.

3.3 Multivariate linear regression

To find out the important determinants of forecast error, a multivariate linear regression analysis of forecast error versus different combinations of features is performed as in

$$y = \beta_0 + \beta_1 x_1 + \cdots + \beta_i x_i + \epsilon. \quad (1)$$

y and x_i represents the RMSE of the forecast and features at a specific forecast hour respectively, β_i is the fit coefficient solved for in the regression analysis, and ϵ is the error term representing the mismatch between the linear model and the observations. The coefficient of determination (R^2) quantifies the goodness of fit and is defined as the ratio of the variance of the regression model and the variance of the observations:

$$R^2 = 1 - \frac{\sum_{i=1}^{m}(y_i - \hat{y}_i)^2}{\sum_{i=1}^{m}(y_i - \bar{y})^2} \times 100\% \quad (2)$$

where $\hat{y}_i$ is the mean modeled y (Eq. 1) and $\bar{y}$ is the mean measured y. The regression is fit to the training data and the results section shows results for an application to the test data (out of sample statistics).

3.4 Analog scheme

To address the limitations of the multivariable linear regression model, an artificial intelligence (AI) method called analog method is also used to estimate the forecast error. The analog of a forecast for a given location and time is defined as a past prediction that matches selected features of the current forecast. Analyzing historical forecasts errors for the analogs, forecast error can be inferred (DelleMonache et al. 2011).

The search for analog forecasts is controlled by a K-nearest neighborhood (KNN) algorithm consisting of a weighted normalized Euclidean distance metric ($\|E\|$) that ranks past predictions by how similar they are to the current forecast

$$\|E\| = \sqrt{\sum_{i=1}^{N} \frac{(F_i - A_i)^2}{\sigma_i}}, \quad (3)$$

where F_i is the current forecast feature value; A_i is the feature value in an analog, *N* is the number of features, σ_i is the standard deviation of each feature in the training dataset respectively.

K analogs (K = 10 here) with the shortest Euclidean distance are then used to predict the error of the current forecast. A weighted average of the analog errors is computed as

$$AN = \sum_{i=1}^{K} \gamma_i E_i, \quad (4)$$

where AN is the weighted average error, E_i is the analog distance in (3), and γ_i is a weight that is inversely proportional to the distance of the analog from the forecast,

$$\gamma_i = \frac{\frac{1}{\|E_i\|}}{\sum_i^K \|E_i\|}. \quad (5)$$

Therefore, a higher weight will be assigned to the analog with the shortest distance from the current forecast.

4. Results

4.1 Forecast performance of different methods

The performance of CMV forecast is compared to the NAM forecast and basic persistence forecast that equates future with current weather condition, i.e. the current kt satellite image is assumed to persist. Forecasts are validated against the truth CLAVR-x kt image. Choosing satellite data as a validation source may artificially increase the NWP and decrease the satellite error, since identical (satellite) and different (NWP) methods are used to determine kt. Comparing forecast results to (independent) ground irradiance measurements would be preferable, but measurement sites are not available at our oceanic site and would also be very sparse over land. The root mean square error between the forecast and truth image is given as

$$RMSE = \sqrt{\frac{\sum_{i=1}^{n}(kt_f - kt_t)^2}{n}}, \quad (6)$$

where kt_f is the forecast kt, kt_t is the truth kt, and n is the number of pixels in an image.

Figure 4 shows the RMSE of kt at different forecast horizons for each forecast model. The NAM forecast error is shown to vary weakly with forecast horizon, which confirmed our earlier assumption. The CMV forecast error increases with increasing forecast horizon as expected. The persistence forecast errors are slightly larger than CMV forecast errors up to a 6 hours forecast horizon. The cross-over time between satellite CMV and NAM forecast is found to be in between forecast horizons of 6 hours and 1 day, which is longer than in Perez et al. (2010) probably because Perez used ground measurements for validation.

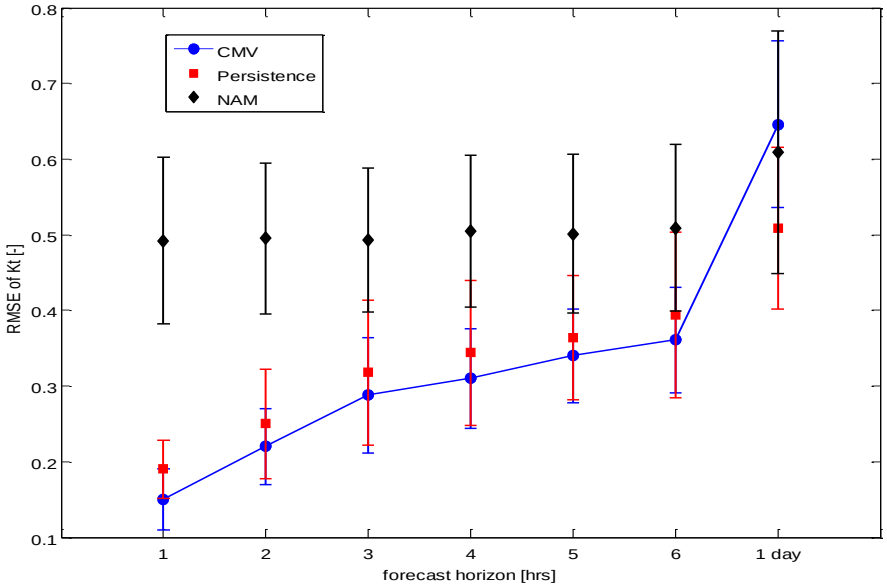

Figure 4. RMSE of kt as a function of forecast horizon for each forecast model. Error bars show the standard deviation of the RMSE. Note the jump from 6 hours to 1 day on the x axis.

159

160 4.2 Satellite forecast RMSE versus kt standard deviation, cloud speed, and
161 cross-correlation coefficient

162 To motivate the analysis in Section 4.3., dependencies of RMSE on a few features are shown in
163 Figs. 5 and 6. The features are computed over 20x20 km (5x5 pixels) rather than the whole region
164 described in section 3.2. Figure 5 shows that RMSE increases with increasing std for all forecast horizons.
165 While RMSE also increases with increasing cloud speed, the increase is smaller (~0.04) than for the std
166 (~0.1). Dependencies between the RMSE and a combination of two features are examined in Fig. 6;
167 RMSE increases with increasing std and decreasing CC. The sensitivity of RMSE to CC increases with std.
168 The R^2 of RMSE vs std, RMSE vs speed, and RMSE vs std and CC for the 1 hour forecast is 36%, 15.8%,
169 and 50.7% respectively.

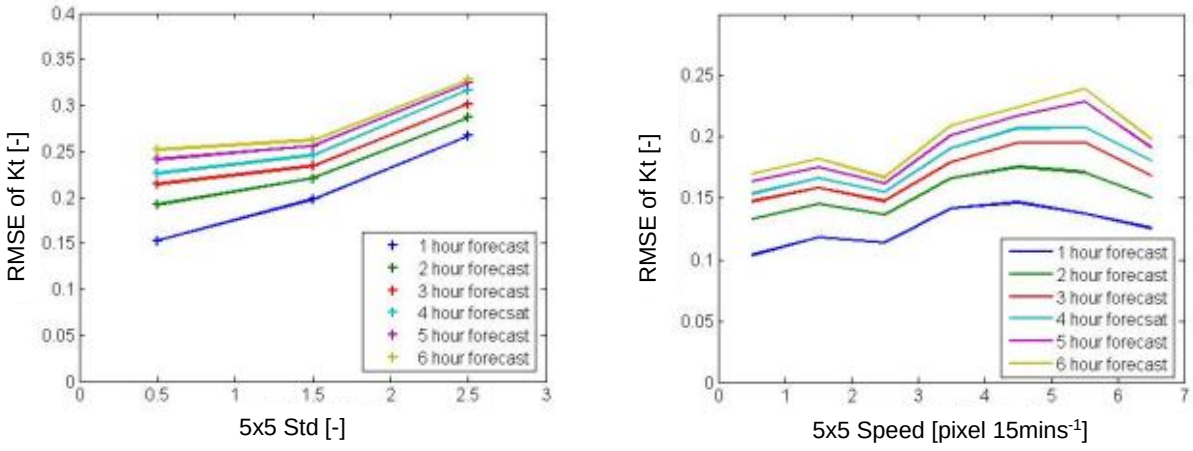

Figure 5. RMSE of kt as a function of std (left) and cloud speed (right) with different forecast horizons (colors).

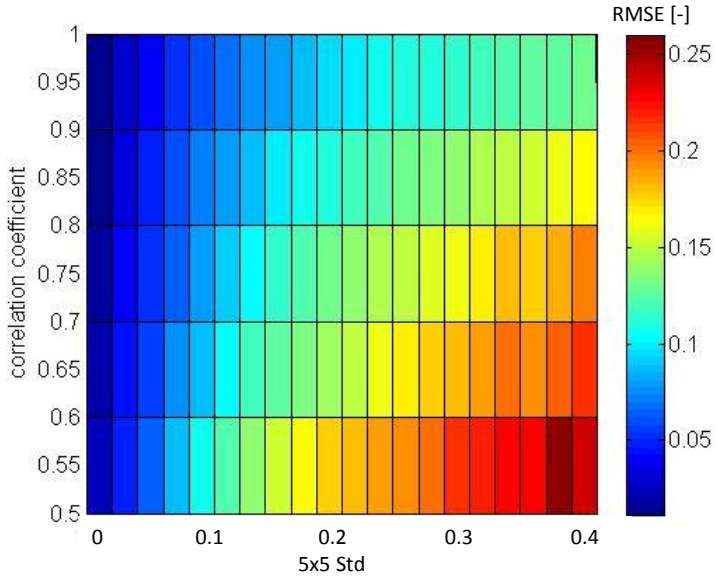

Figure 6. RMSE of kt (colorbar) as a function of std and CC for the 1st hour of CMV forecast.

4.3 Multivariate linear regression for satellite forecast RMSE

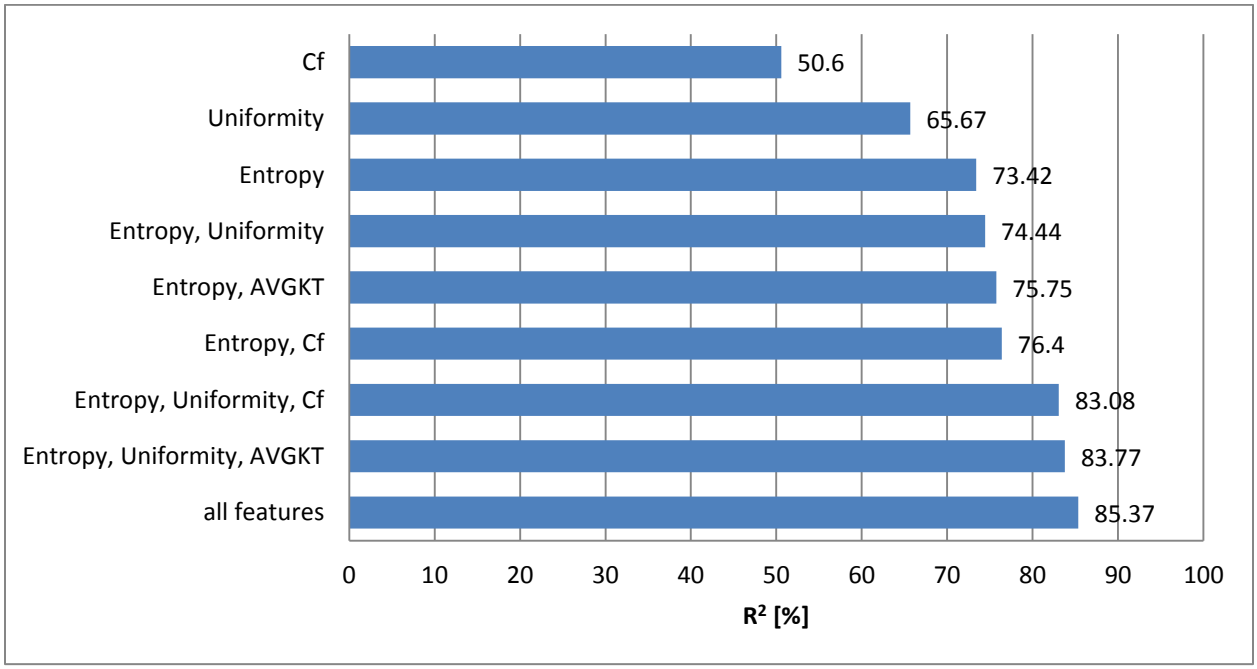

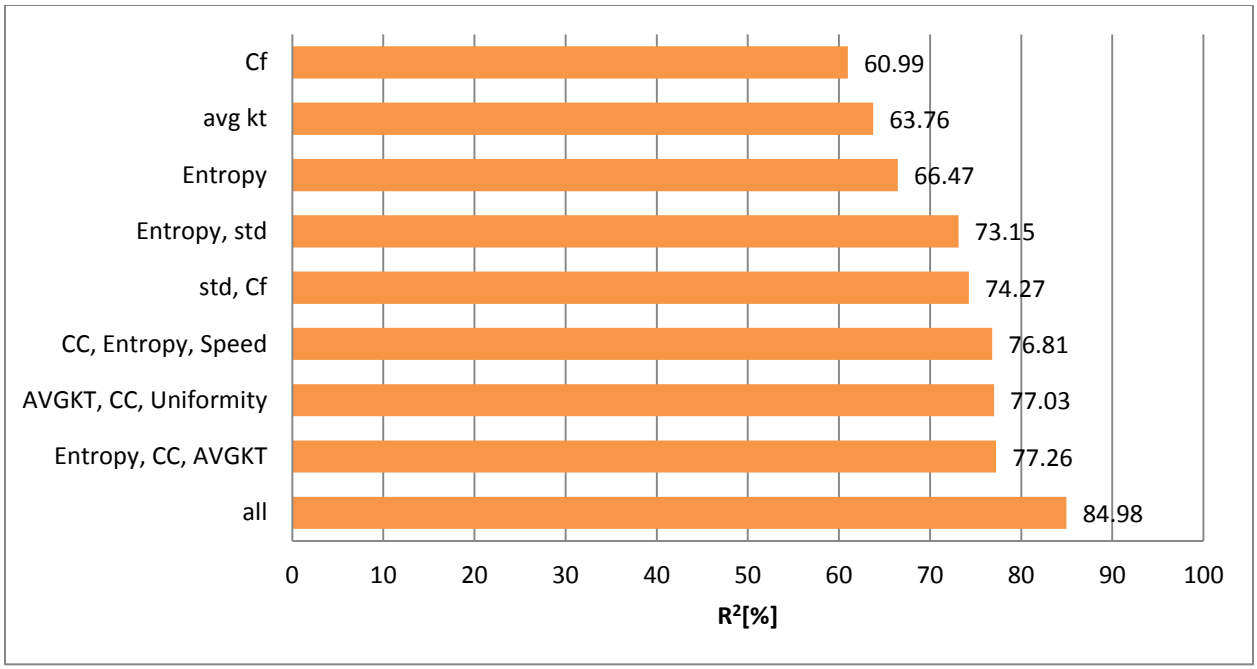

Figure 7. Coefficient of determination (R^2) for different combination of features for the 1st hour (top) and the 5th hour of CMV forecast (bottom).

Figure 7 shows the coefficient of determination (R^2) for several multivariate linear models (Eq. 1) at different forecast horizons, each representing a different combination of features. R^2 describes the goodness of multivariate linear fit of RMSE. For the first forecast hour RMSE modeled with a single feature, the satellite forecast RMSE is most correlated to Entropy (R^2=73.4%), followed by Uniformity (R^2=65.7%). For two features, the highest correlated combination of features is Entropy and cloud fraction with a 3% increase (R^2=76.4%) compared to the single feature using Entropy. R^2 further increases to 83% with a combination of Entropy, Uniformity and Cf or AVGKT. Adding extra variables only slightly increases R^2 to 85.4%. The R^2 for single and double feature model has a similar trend for forecast horizons of 1-3 hours. While cloud speed replaces Cf or AVGKT in triple variable models to become the highest correlated combination, the difference in R^2 is not significant. Entropy and Uniformity are the most important features for 1-3 hour forecasts.

At the fourth to sixth hour of forecast, the combination of important features changes (Fig. 7 bottom). Entropy is still the feature with the largest R^2. The combination of CC, AVGKT, and Entropy or Uniformity is found to have the highest correlation. Since entropy and uniformity are correlated and cloud fraction is correlated to AVGKT, the main difference between the 1-3 hours and 4-6 hours models is that CC has a larger impact on the forecast RMSE for longer (> 3 hours) forecast horizon.

The multivariate regression analysis suggests that Entropy (i.e. the randomness of the kt field, Fig. 3) is the primary predictor of CMV forecast RMSE. A high randomness typically indicates that the cloud pattern is made of many small scale clouds or clouds with high spatial variability of optical thickness. Since smaller scale clouds tend to have a smaller 'half-life' than large clouds, the assumption of a 'frozen' cloud field in the CMV method is violated, resulting in larger forecast error.

4.4 Predicting CMV versus NAM forecast performance

To demonstrate the performance of both predictive models, forecasts for May 25th - June 25th, 2012 are analyzed using April 24 – May 24, 2012 as the training period. The RMSE predicted by the linear regression method in Eq. 1 and the weighted analog in Eq. 4 are validated against the truth RMSE. The relative RMSE (rRMSE) of each model is computed as

$$rRMSE_{model} = \frac{1}{RMSE_{mean}} \sqrt{\frac{\sum_{i=1}^{n}(\mathrm{RMSE}_{predicted} - RMSE_{truth})^2}{n}} \times 100\% \quad (7)$$

where $RMSE_{mean}$ is the mean of the truth RMSE.

To compare the predictability of errors of different forecasts, the relative performance (RP) is used:

$$RP_{NAM,i} = \frac{RMSE_{NAM,i}}{RMSE_{CMV,i}}, \quad (8)$$

where i indicates forecast horizon. The idea of RP is similar to the cross-over time mentioned earlier. RP describes the relative performance of two models in terms of RMSE at a particular forecast horizon: RP < 1 indicates that CMV performs better than the NAM forecast, and vice versa. Under certain conditions, a cross-over time (RP = 1) earlier than the one in Fig. 4 can be found (Fig. 8).

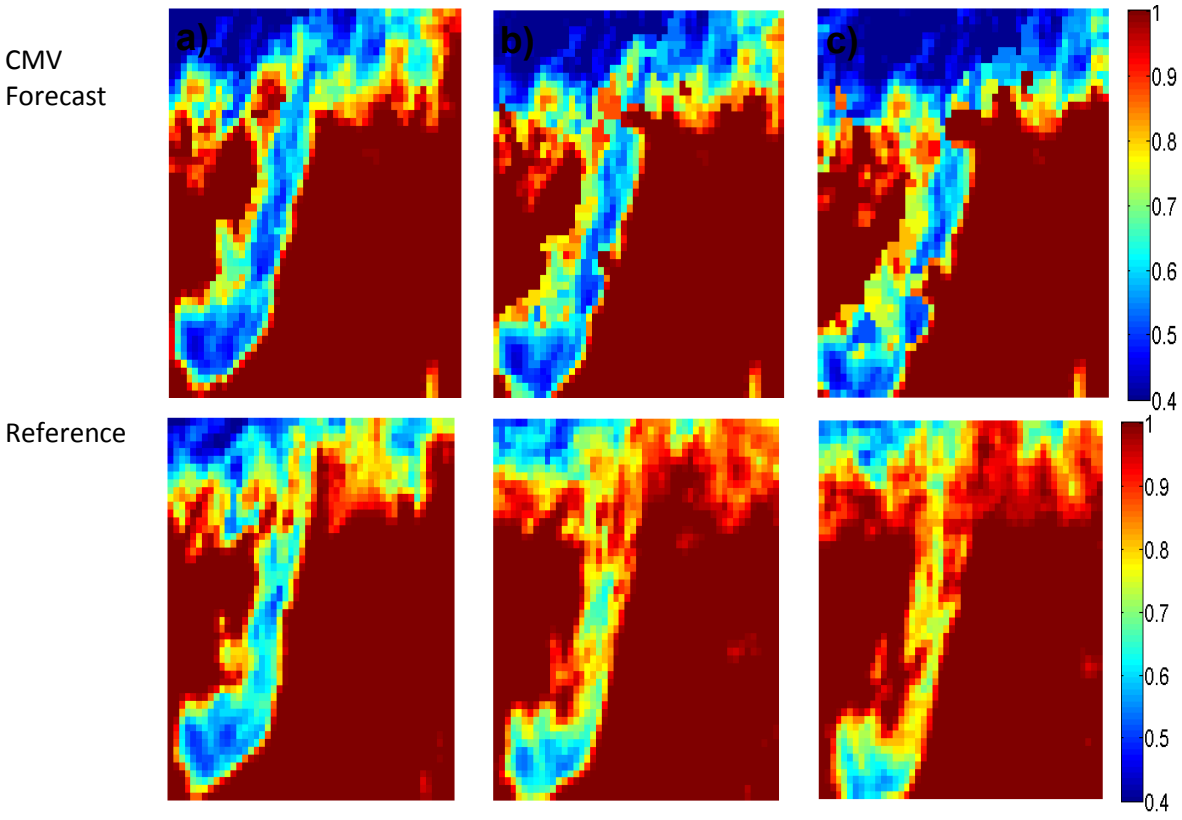

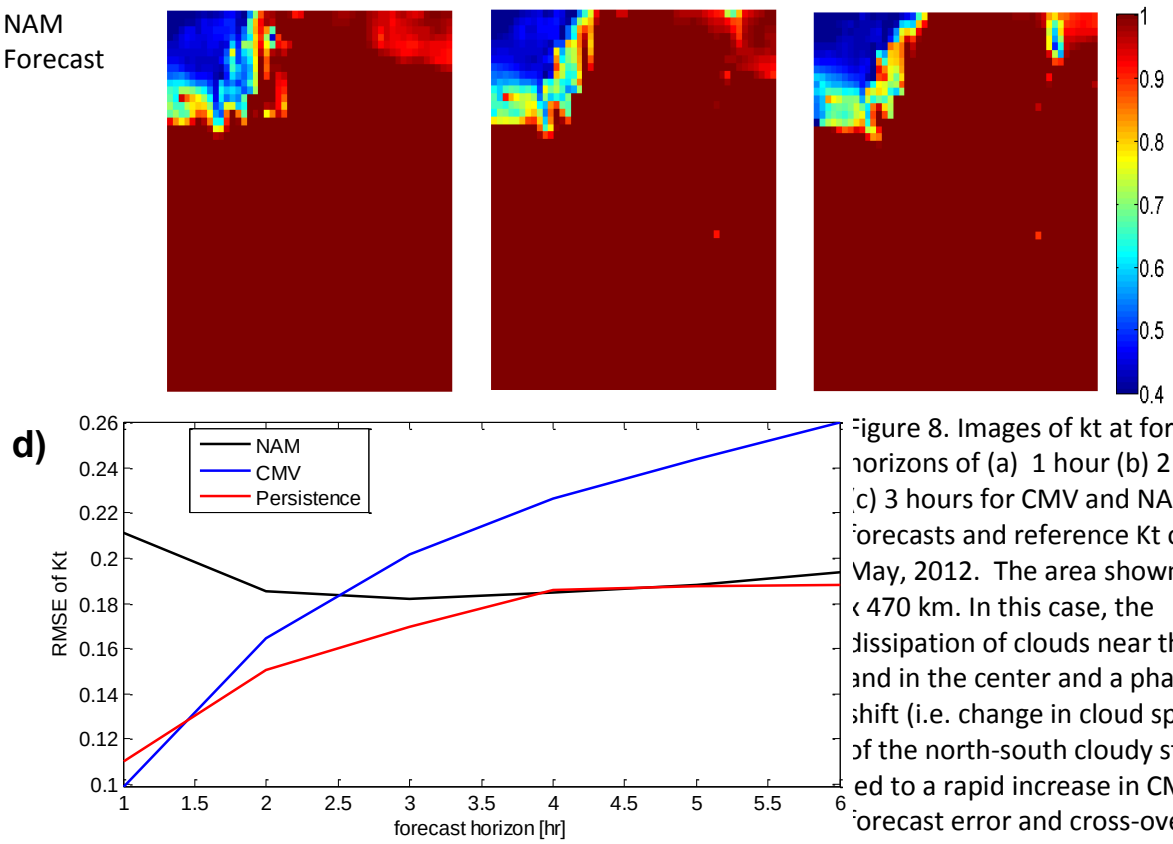

Figure 8. Images of kt at forecast horizons of (a) 1 hour (b) 2 hours (c) 3 hours for CMV and NAM forecasts and reference Kt on 27th May, 2012. The area shown is 234 x 470 km. In this case, the dissipation of clouds near the top and in the center and a phase-shift (i.e. change in cloud speed) of the north-south cloudy stripe led to a rapid increase in CMV forecast error and cross-over with the NAM forecast at 2.5 hours (d).

Table 2 shows a comparison of the performance of the multivariate regression and analog method in predicting CMV forecast error and RP. The analog method is shown to outperform the multivariate linear regression method with the best combination of features (largest R^2) for both predicting CMV forecast error and RP_{NAM}. The average rRMSE of predicting CMV forecast error is 14.4% and 23.9% for analog and regression method respectively, while the average rRMSE of predicting RP_{NAM} is 27.6% and 31.7%. The errors of both methods are found to be independent of the forecast horizon. Satellite image Uniformity is observed to be the most important feature for predicting the RP_{NAM}. The impact of other features varies by forecast horizon.

Table 2. Predicted CMV forecast error and RP with analog and multivariate linear regression model. Training data is from April 24 - May 24 and test data is May 25 – June 25, 2012.

	Predicted CMV forecast error		Predicted RP_{NAM}	
Forecast hour	$rRMSE_{analog}$	$rRMSE_{regression}$	$rRMSE_{analog}$	$rRMSE_{regression}$
1	16.5%	21.4%	31.2%	37.3%
2	13.0%	28.6%	27.2%	30.6%
3	13.5%	19.7%	20.3%	27.2%
4	15.6%	23.5%	29.6%	31.0%
5	14.0%	23.2%	30.3%	35.1%
6	13.9%	27.1%	27.1%	29.0%

5. Conclusions

A technique for solar forecasting using satellite imagery with the ability to characterize and predict the forecast error using multivariate linear regression and the analog model is presented. CMV solar forecasts are computed using the cross-correlation algorithm applied pixel-by-pixel with CLAVR-x processed GOES-15 cloud transmissivity for one month. On average, the RMSE is found to increase with increasing forecast horizon for both persistence and CMV forecast and becoming large than NAM forecast error (i.e. with a cross-over time) at forecast horizons between 6 hours and 1 day.

The dependence of forecast RMSE on different features is analyzed using multivariate linear regression and analog models. Entropy is shown to contribute the most to the CMV forecast RMSE. The rRMSE of predicting CMV forecast error is found to be 14.4% for the analog model and 23.9% for the regression model. This indicates that the CMV model errors show a non-linear dependence on the selected features that can be better captured by the analog method versus a linear regression.

The relative performance of NAM and satellite CMV models is also analyzed. Based on Fig. 4, RP decreases from about 3.5 at the first forecast hour to 1.5 at the 6th forecast hour, on average. The cross-over time (when CMV becomes less accurate than numerical weather prediction forecasts) is found to be more than 6 hours, on average, but as early as 2 hours under certain conditions. The rRMSE of predicting RP is shown to be 27.6% and 31.7% for analog and regression method respectively. Consequently, both models have skill in informing forecasters at what forecast horizon a numerical weather prediction forecast should start to be used instead of a satellite forecast.

With only two months of available CLAVR-x data, the model performance is limited by the data size being used to train the models. Especially for the analog method a larger training data set increases the chance to find similar analogs improving model accuracy.

Table 3 shows the pipeline of operational satellite CMV forecast and the processing time for each step using a desktop computer. Using this strategy an operational forecast can be provided within less than 25 minutes after satellite image capture.

Table 3. Pipeline of CMV forecast and the processing time for each step

Procedures	Processing time
Download and extract GOES15 data from CLARV-x	20 min
Compute cloud motion vectors	40 sec
Advect kt pixels and register forecast images out to 6 hours	20 sec
Predict errors and RP of CMV and NAM	90 sec
Total	23.5 min

References

DelleMonache, L., Nipen, T., Liu, Y., Roux, G., Stull, R., 2011: Kalman filter and analog schemes to post-process numerical weather predictions. Monthly Weather Review, in press.

Fujita, T., 1968: Present status of cloud velocity computations from ATS-1 and ATS-3. COSPAR Space Res., 9, 557-570

241 Hammer, A., Heinemann, D., Hoyer, C., Kuhlemann, R., Lorenz, E., Müller, R. and Beyer, H. G. (2003):
242 Solar Energy Assessment Using Remote Sensing Technologies. Remote Sensing of Environment 86, 423–
243 432.
244 Haralick, Robert M., and Linda G. Shapiro, Computer and Robot Vision, Volume II, Addison-Wesley, 1992,
245 pp. 316-317
246 Ineichen, P., Perez R., 2002.A new airmass independent formulation for the Linke turbidity coefficient.
247 Solar Energy, 73(3), 151–157.
248 Lorenz, E., Hurka, J., Heinemann, D., Beyer, H., 2009. Irradianceforecasting for the power prediction of
249 grid-connected photovoltaicsystems.IEEE Journal of Selected Topics in Applied Earth Observa-tions and
250 Remote Sensing 2 (1), 2–10.
251 Marquez R., H.T.C. Pedro and C.F.M. Coimbra (2012), Hybrid ANN/Satellite Imaging Forecasting Method
252 for Global Horizontal Irradiance," submitted to Solar Energy.
253 Mathiesen, P., Kleissl, J., 2011. Evaluation of numerical weatherprediction for intra-day solar forecasting
254 in the CONUS. Sol. Energy85 (5), 967–977.
255 Mecikalski, J. R. 2002. Using cloud-motion winds to understand kinematic processes of deep convection:
256 Anvil-level outflow and momentum transport. *Proc. Sixth Int. Winds Workshop*, Madison, WI, WMO, 97–
257 104.
258 Nieman, S. J., W. P. Menzel, C. M. Hayden, D. Gray, S. T. Wanzong, C. S. Velden, and J. Daniels, 1997:
259 Fully automated cloud-drift winds in NESDIS operations. Bull. Amer. Meteor Soc., 78, 1121-1133.
260 Pavolonis, Michael J.; Heidinger, Andrew K. and Uttal, Taneil. 2005: Daytime global cloud typing from
261 AVHRR and VIIRS: Algorithm description, validation, and comparisons. Journal of Applied Meteorology,
262 Volume 44, Issue 6, 2005, pp.804-826.
263 Pavolonis, Michael J. and Heidinger, Andrew K.. 2004: Daytime cloud overlap detection from AVHRR and
264 VIIRS. Journal of Applied Meteorology, Volume 43, Issue 5, 2004, pp.762-778.
265 Perez, R., S. Kivalov, J. Schlemmer, K. Hemker Jr., D. Renne and T. Hoff, (2010): Validation of short and
266 medium term operational solar radiation forecasts in the US. Solar Energy (in press).
267 Perez, R., M. Beauharnois, K. Hemker Jr., S. Kivalov, E. Lorenz, S. Pelland, J. Schlemmer, and G. Van
268 Knowe, (2011): Evaluation of Numerical Weather Prediction Solar Irradiance Forecasts in the US. Proc.
269 Solar 2011, American Solar Energy Society's Annual Conference.
270 Rabin, R. M., S. F.Corfidi, J. C.Brunner, and C. E.Hane.2004. Detecting winds aloft from water vapor
271 satellite imagery in the vicinity of storms. Weather 59:251–257.
272 Velden, C. S., C. M. Hayden, S. J. Nieman, W. P. Menzel, S. Wanzong, and J. S. Goerss. 1997. Upper-
273 tropospheric winds derived from geostationary satellite water vapor observations. Bull. Amer. Meteor.
274 Soc. 78:173–195.
275 Velden, C. S., T. L. Olander, and S. Wanzong. 1998. The impact of multispectral GOES-8 wind information
276 on Atlantic tropical cyclone track forecasts in 1995. Part I: Dataset methodology, description, and case
277 analysis. Mon. Wea. Rev. 126:1202–1218.
278 WRF, 2010.Weather Research and Forecasting (WRF) Model.<http://www.wrf-model.org>.